

Article

Application of Biobased Substances in the Synthesis of Nanostructured Magnetic Core-Shell Materials

Marcos E. Peralta ^{1,*}, Alejandro Koffman-Frischknecht ¹, M. Sergio Moreno ², Daniel O. Mártire ³
and Luciano Carlos ^{1,*}

¹ Instituto de Investigación y Desarrollo en Ingeniería de Procesos, Biotecnología y Energías Alternativas, PROBIEN (CONICET-UNCo), Universidad Nacional Del Comahue, Neuquén 8300, Argentina

² Instituto de Nanociencia y Nanotecnología, INN (CNEA-CONICET), Centro Atómico Bariloche, Av. Bustillo 9500, San Carlos de Bariloche 8400, Argentina

³ Instituto de Investigaciones Físicoquímicas Teóricas y Aplicadas (INIFTA), CCT-La Plata-CONICET, Universidad Nacional de La Plata, La Plata 1900, Argentina

* Correspondence: marcos.peralta@probien.gob.ar (M.E.P.); luciano.carlos@probien.gob.ar (L.C.)

Abstract: We propose here a novel green synthesis route of core-shell magnetic nanomaterials based on the polyol method, which uses bio-based substances (BBS) derived from biowaste, as stabilizer and directing agent. First, we studied the effect of BBS concentration on the size, morphology, and composition of magnetic iron oxides nanoparticles obtained in the presence of BBS via the polyol synthesis method (MBBS). Then, as a proof of concept, we further coated MBBS with mesoporous silica (MBBS@mSiO₂) or titanium dioxide (MBBS@TiO₂) to obtain magnetic nanostructured core-shell materials. All the materials were deeply characterized with diverse physicochemical techniques. Results showed that both the size of the nanocrystals and their aggregation strongly depend on the BBS concentration used in the synthesis: the higher the concentration of BBS, the smaller the sizes of the iron oxide nanoparticles. On the other hand, the as-prepared magnetic core-shell nanomaterials were applied with good performance in different systems. In particular, MBBS@SiO₂ showed to be an excellent nanocarrier of ibuprofen and successful adsorbent of methylene blue (MB) from aqueous solution. MBBS@TiO₂ was capable of degrading MB with the same efficiency of pristine TiO₂. These excellent results encourage the use of bio-based substances in different types of synthesis methods since they could reduce the fabrication costs and the environmental impact.

Keywords: magnetic nanoparticles; magnetite; solvothermal synthesis; waste valorization; green chemistry



Citation: Peralta, M.E.;

Koffman-Frischknecht, A.; Moreno, M.S.; Mártire, D.O.; Carlos, L.

Application of Biobased Substances in the Synthesis of Nanostructured Magnetic Core-Shell Materials.

Inorganics **2023**, *11*, 46. <https://doi.org/10.3390/inorganics11010046>

Academic Editor: Carlos Martínez-Boubeta

Received: 29 November 2022

Revised: 11 January 2023

Accepted: 12 January 2023

Published: 16 January 2023



Copyright: © 2023 by the authors. Licensee MDPI, Basel, Switzerland. This article is an open access article distributed under the terms and conditions of the Creative Commons Attribution (CC BY) license (<https://creativecommons.org/licenses/by/4.0/>).

1. Introduction

Nowadays, magnetic nanoparticles and nanostructured magnetic materials with core-shell type structure are attracting widespread interest in material science due to their potential applications in many fields, including environmental remediation, drug delivery, magnetic resonance imaging, electronics, sensor developments, etc. [1]. Additionally, there are several new applications of magnetic nanoparticles and nanomagnetic fluids such as temperature sensors, heat exchangers, magnetic actuators, and energy harvesters that open up new possibilities for the development of these fields [2–4]. Among the magnetic nanomaterials, magnetic iron oxide nanoparticles (IONPs) (e.g., magnetite, Fe₃O₄, and maghemite, γ-Fe₂O₃), have been widely studied due to their superparamagnetic behavior and because they are more environmentally friendly compared to other metals such as the Co and the Ni. [5,6]. Different methodologies have been implemented to prepare IONPs, such as coprecipitation, micelle synthesis, sol-gel method, thermal decomposition, and polyol method [7]. Among these synthetic methods, the polyol method is a well-suited technique to obtain pure and monodispersed nanoparticles with a narrow and controllable size distribution [8]. In this method, ferric salts mixed with a stabilizer are dissolved in a solvent, such as glycols (e.g.,

ethylene glycol or diethylene glycol), and heated to the boiling point of the solvent. The stabilizers are normally surfactants or polymers, whose main function is to regulate the size of the primary nanocrystals and secondary aggregates [9]. Various substances were studied as stabilizer including sodium citrate [10–12], polyethylene glycol (PEG) [13], polyacrylic acid (PAA) [14–16], polyvinylpyrrolidone (PVP) [17], cetyltrimethylammonium bromide (CTAB) [9], and sodium dodecyl benzene sulfonic acid (SDBS) [15]. However, a major drawback of using some synthetic surfactants is their lack of biodegradability or biocompatibility (e.g., PAA), or their toxicity (e.g., CTAB and SDBS), what discourages their applications.

The replacement of synthetic stabilizer with substances deriving from the treatment of biowaste is considered as a green process since it values waste as a source of renewable raw material for the synthesis of new technological materials, which leads to a reduction in the manufacturing costs and environmental impact. Aerobic biodegradation of the wet organic fraction of municipal waste has been shown to yield polymeric bio-based substances (BBS), which have chemical similarities to humic substances and possess surfactant properties which make them suitable as green auxiliary synthesis reactants [18,19]. In particular, BBS were used in the synthesis process of different materials as a structure directing agent in the preparation of mesoporous silica nanoparticles due to their ability to form micelles [20], as sacrificial carbon in the formation of zero-valent iron nanoparticles from carbothermal synthesis [21], and as stabilizer for the generation of silver nanoparticles [22]. On the other hand, BBS-coated magnetic nanoparticles and magnetic nanocomposites prepared using BBS have been successfully employed as adsorbents [23–25], photo-Fenton catalysts [26], and photocatalysts [27,28] for water treatment processes. However, the role of BBS as synthesis aids in the polyol method for the preparation of IONPs has not been addressed. Furthermore, since BBS could act as both nucleation directing agents and structure directing agents, they may play a critical role in the synthesis of nanostructured magnetic core-shell materials.

This paper investigates the possible application of BBS as green aids to act as stabilizers in the preparation of IONPs via polyol synthesis method and as nucleation directing agents in the synthesis of nanostructured core-shell magnetic oxide particles. For the latter, the as-prepared BBS-modified IONP nanoparticles were coated with mesoporous SiO₂ and TiO₂, and two types of magnetic core-shell structured nanoparticles, MBBS@mSiO₂ and MBBS@TiO₂, were prepared. Finally, the performance of nanostructured magnetic core-shell nanoparticles in specific applications was evaluated. The potential application of BBS in the preparation of nanomaterials opens up new ways for the development of novel synthesis strategies and represents an economically sustainable method of waste valorization.

2. Results and Discussion

2.1. Synthesis of IONPs Using BBS

First, IONPs without BBS (Fe₃O₄) and with different amounts of BBS (35 mg, 70 mg, 200 mg, 500 mg and 1000 mg) were prepared via the polyol method. The obtained nanoparticles were called MBBS-X, where X stand for the mass of BBS used in the synthesis. The morphology of MBBS was studied by TEM images. Bare magnetite (Figure 1A) consists of spherical nanoparticles with a mean diameter of circa 80 nm with wide particle size distribution and poor dispersity. Figure 1B–D shows typical TEM images of the samples obtained with different BBS loads. It can be observed that the size of the nanocrystals and the secondary aggregates (or clusters) depend on the BBS concentration used in the synthesis. A particle size distribution obtained from the TEM images for each material is shown in Figure S1, Supplementary Materials. In particular, for MBBS-35 particles (Figure 1B), well-defined roughly spherical clusters with diameters of about 70–200 nm are observed. The clusters are composed of self-assembled small primary nanocrystals and an outer layer of organic matter less than 10 nm thick, as estimated from the lighter shell surrounding the cluster (Figure S2, Supplementary Materials). In sample MBBS-200, clusters with less geometrical shape are observed (Figure 1C). As the concentration of BBS increases, large aggregates of small IONPs are observed without a defined shape (e.g., sample MBBS-1000,

Figure 1D). Additionally, sample MBBS-1000 showed IONPs with the smallest particle size, which were around 5 nm (Figure S3, Supplementary Materials). These results suggest that BBS regulates the size of IONPs by limiting the growth of nanoparticles, the higher the concentration of BBS, the smaller the sizes of the IONPs. Furthermore, at high BBS concentration, BBS coated the majority of small IONPs, which avoids the formation of spherical cluster.

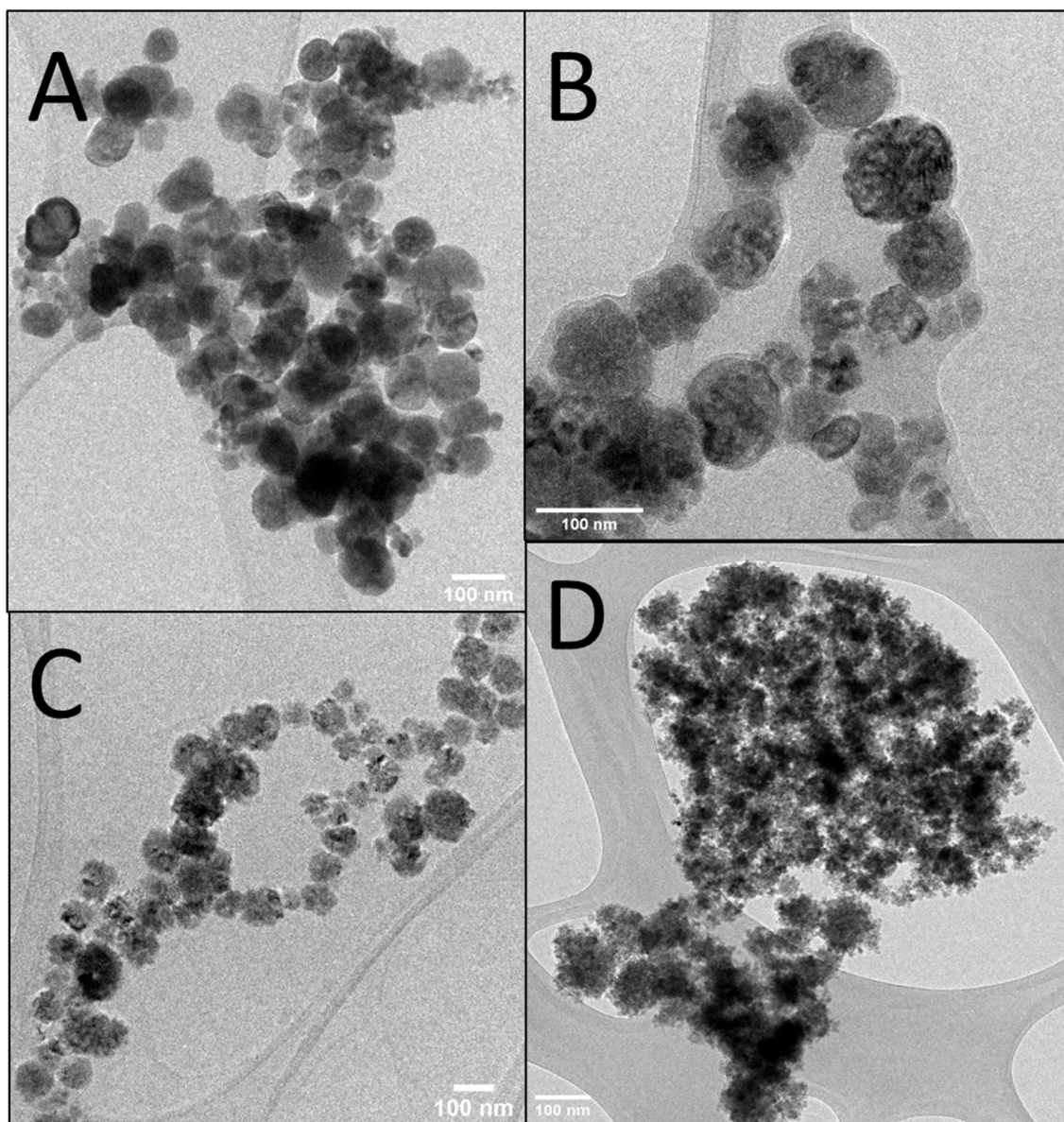


Figure 1. TEM images of Fe₃O₄ (A), MBBS-35 (B), MBBS-200 (C) y MBBS-1000 (D).

In order to characterize the presence of BBS on the surface of the obtained IONPs, FTIR spectra were performed (Figure 2A). The band at 1080 cm⁻¹ (ν_{C-O}), associated with organic matter, increases in intensity with the amount of BBS. The carboxylate group band (1620 cm⁻¹) and the carboxylate-iron stretching signal (1400 cm⁻¹) [29] are observed in all spectra, which suggests that carboxylate groups indeed play an important role in the bonding of the BBS to the IONPs surface. This result is in agreement with previous reports obtained for BBS-coated Fe₃O₄ nanoparticles prepared via the coprecipitation method [23]. The presence of carboxylate bands in the Fe₃O₄ spectrum could be due to the fact that sodium acetate was not completely removed in the washing steps. In the lower frequency FTIR region, the samples showed characteristic signals assigned to Fe-O

bonds. The broad band in the range of 500–800 cm^{-1} is due to the stretching vibration of the Fe-O in tetrahedral sites (ν_1) [30]. The ν_1 frequency for Fe_3O_4 is observed at 567 cm^{-1} . It is important to note that this vibration mode was broadened after BBS coating and at high BBS amounts a splitting is observed, which might be due to symmetry lowering [31]. The broadening is due to the statistical distribution of cations over the octahedral and tetrahedral sites, while the local symmetry is disturbed [32]. Taking this into account, we propose that the interaction of BBS with surface Fe atoms induces a change in the local symmetry of the outer tetrahedral sites likely to result in peak broadening.

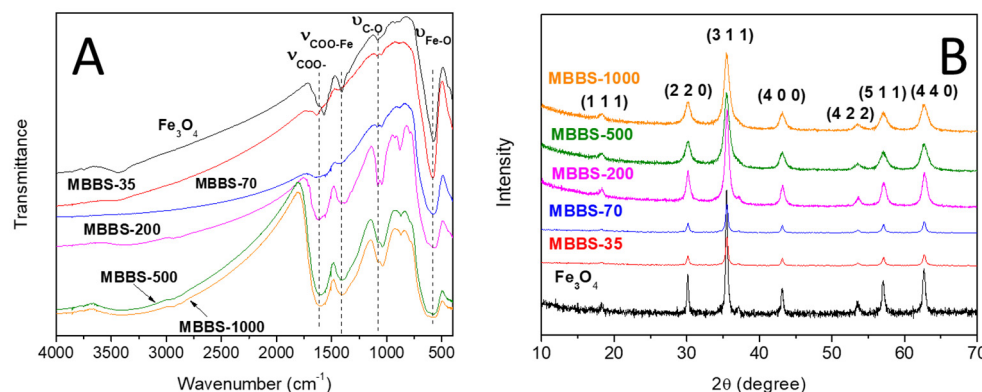


Figure 2. (A) FTIR spectra of MBBS nanoparticles. The main relevant peaks are labeled. (B) XRD diffraction patterns of MBBS nanoparticles. The indexed labels identify the miller indices of the Fe_3O_4 phases.

The XRD patterns of MBBS (Figure 2B) were recorded to determine the crystalline phases present in the nanoparticles. All diffractograms are very similar and show main diffraction peaks in good agreement with a reference pattern of magnetite. In particular, the XRD peak positions at 30.1 (220), 35.4 (311), 43.1 (400), 53.4 (422), 56.9 (511), and 62.5 (440) perfectly match with the lattice planes of magnetite (Card number 01-075-1610, ICDD Database). The phase identification of magnetite and maghemite by the conventional X-ray diffraction method is not a simple matter because both have the same cubic structure and their lattice parameters are almost identical [33]. However, the presence of doublets at the high-angle peaks as (5 1 1) and (4 4 0) is indicative of the presence of magnetite and maghemite in the samples [34]. Furthermore, a decrease in the lattice constant for the peaks (5 1 1) and (4 4 0) of magnetite is also indicative of the formation of maghemite [35]. For MBBS samples, a two-peak convolution was not noticed for the (5 1 1) and (4 4 0) planes and we did not observe any decrease in the lattice constant for the (5 1 1) and (4 4 0) peaks with respect to the Fe_3O_4 nanoparticles prepared without BBS. Therefore, this could indicate that in our samples Fe_3O_4 is the main phase of magnetic iron oxide, however, the presence of a small amount of maghemite cannot be ruled out. No other crystalline materials are detected, which indicates that BBS act as good stabilizer to obtain IONPs via the polyol method.

In order to determine the quantity of organic matter in MBBS samples, a thermogravimetric analysis (TGA) was performed. The amount of organic matter was calculated by measuring the total mass loss up to 1000 $^{\circ}\text{C}$ (Table S1, Supplementary Materials). As can be seen in Figure 3A, the BBS loading on the IONPs increases with the amount of BBS used in the synthesis, reaching the maximum value of near 47.2 wt.%.

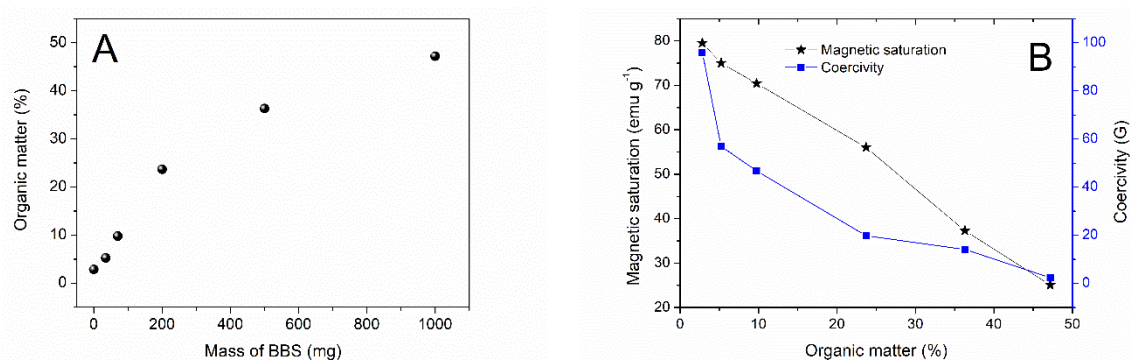


Figure 3. (A) Total organic matter (%) determined from the TGA vs. Mass of BBS used during synthesis (mg) for MBBS samples; (B) magnetization of saturation (emu g^{-1}) and Coercivity as a function of organic matter (%) determined from the TGA for MBBS samples.

The magnetic properties of MBBS samples and bare magnetite were evaluated by magnetization curves (Figure S4 and Table S2, Supplementary Materials). Magnetic saturation values (M_s) decrease with an almost linear relationship with the BBS loading (Figure 3B). The decrease in the saturation magnetization may be due to the non-magnetic fraction as well as the reduction in particle size. It is important to note that the larger the BBS loading, the smaller the coercivity (Figure 3B). This is due to the particles approaching superparamagnetism with size reduction [36,37]. For spherical magnetite nanoparticles, the critical superparamagnetic size is 26 nm [36], thus samples with high BBS content lead to superparamagnetic behavior. These results evidence the critical role of the adsorbed BBS on the magnetic properties of the IONPs.

Zeta potential values of bare magnetite and BBS coated IONPs measured in 10^{-2} M KCl aqueous solutions at pH 3, 6, and 10 are shown in Table S3, Supplementary Materials. The isoelectric point of Fe_3O_4 nanoparticles is 7.2 [38], which indicates that at lower pH values it presents positive charge. Because BBS is negatively charged in the range of pH 3–10, the positive charge observed for MBB-35 and MBB-70 at pH 3 could be the consequence of the limited covering of the IONPs surface by BBS. However, when higher amounts of BBS are used (i.e., MBB-200, MBB-500, and MBB-1000), a negative charge on the surface of the nanoparticles is observed over all the three pH values (3, 6, 10). Additionally, zeta potential becomes more negative as the pH increases because of the dissociation of carboxylic and phenolic groups of BBS [23].

2.2. MBBS@mSiO₂ and MBBS@TiO₂ Nanoparticles

In order to evaluate the role of BBS as a nucleation directing agent in the synthesis of nanostructured core-shell magnetic oxide particles, IONPs were coated directly by two types of common inorganic materials, mesoporous silica (mSiO₂) and titanium dioxide (TiO₂). Due to its magnetic properties, cluster size and particle size distribution we selected MBBS-35 for the synthesis of core-shell nanomaterials, which were named MBBS@mSiO₂ and MBBS@TiO₂. As control experiments, the synthesis of core@shell magnetic nanoparticles was performed with Fe_3O_4 nanoparticles prepared in the absence of BBS. No core@shell structure was formed, either for mSiO₂ or for TiO₂, when the IONP nanoparticles without BBS were used in the synthesis (data not shown). On the contrary, TEM images of MBBS@mSiO₂ show that the material consists of nanoparticles of spherical morphology with a dark core (iron oxide) covered by a quite uniform lighter porous shell (mesoporous silica) of c.a. 20 nm in thickness (Figure 4). This result evidences that BBS plays an important role in the growth of the mSiO₂ layer on the surface of IONPs. It is likely that the negatively charged carboxylate groups on MBBS surface interact with the positively charged CTAB molecules leading to the growth of the mesoporous silica layer onto the BBS-coated IONPs. FTIR spectra (Figure S5, Supplementary Materials) also support the presence of silica on the surface of IONPs. The wide band with a peak at around 1084 cm^{-1}

is associated with the stretching vibration of the Si–O–Si bond from the silica framework. The peak at 571 cm^{-1} corresponds to Fe–O stretching, whereas the bands at 3430 cm^{-1} and 1632 cm^{-1} can be associated with O–H stretching and H–O–H bending vibrations from absorbed water. The XRD pattern of MBBS@mSiO₂ (Figure 5A) indicates that the IONPs did not undergo any crystalline transformation to non-magnetic iron oxide phases during the mSiO₂ synthesis step and its subsequent calcination. The broad peak at around $2\theta = 24^\circ$ is assigned to the halo pattern of amorphous SiO₂ [39].

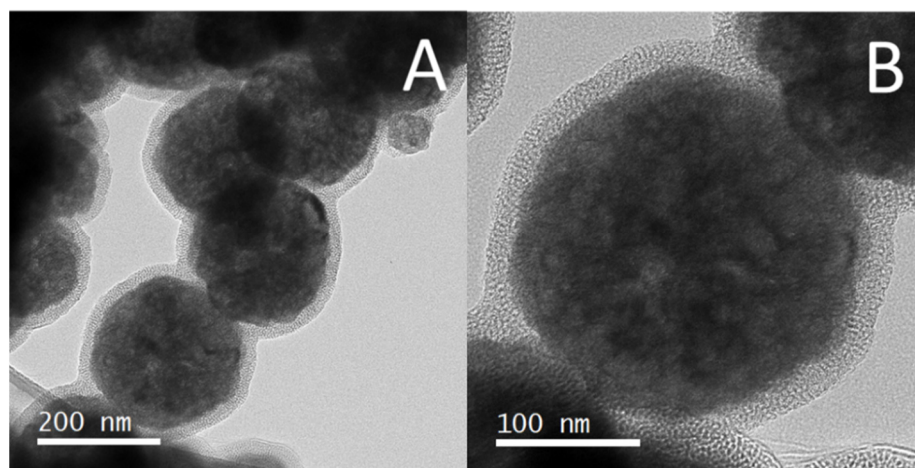


Figure 4. (A,B) TEM images of MBBS@mSiO₂.

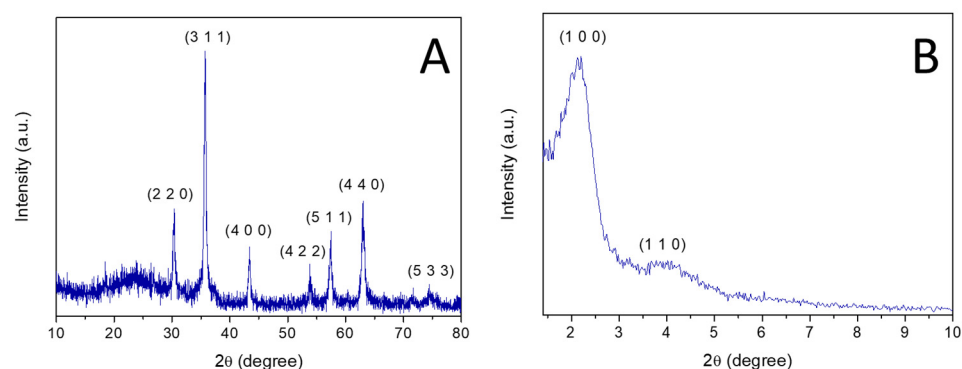


Figure 5. Wide-angle XRD patterns (A) and small-angle XRD (B) patterns of MBBS@mSiO₂. The indexed labels identify the miller indices of the Fe₃O₄ phases (A) and Bragg reflections of MCM-41 (B).

The small-angle XRD patterns of MBBS@mSiO₂ (Figure 5B) exhibit an intense peak at about $2\theta = 2.2^\circ$ and a weak peak at $2\theta = 3.9^\circ$, which correspond to (100) and (110) Bragg reflections of MCM-41 according to previous reports [40,41]. This suggests a well-ordered hexagonal array of mesopores. The porous structure of silica shell was further investigated by the N₂ adsorption–desorption technique (Figure S6A, Supplementary Materials). The N₂ adsorbed quantity, the specific surface area (S_{BET}), and the pore volume (P_V) resulted to be higher for MBBS@mSiO₂ ($S_{\text{BET}} = 136\text{ m}^2\text{ g}^{-1}$, $P_V = 0.135\text{ cm}^3\text{ g}^{-1}$) compared to MBBS-35 ($S_{\text{BET}} = 23\text{ m}^2\text{ g}^{-1}$, $P_V = 0.056\text{ cm}^3\text{ g}^{-1}$). This result is consistent with a mesoporous shell covering MBBS-35. MBBS@mSiO₂ displays type IV isotherms and H4 hysteresis loop according to IUPAC classification [42]. This behaviour can be related to the presence of pores in the mesopore range, as well as other pores with bigger diameters [43]. However, BJH pore size distribution (Figure S6B, Supplementary Materials) only shows a uniform mesoporous size of 2.9 nm, thus the larger pore size could be due to particle aggregation.

Magnetic hysteresis curve at room temperature of MBBS@mSiO₂ is shown in Figure S7, Supplementary Materials. MBBS@mSiO₂ still displays a superparamagnetic behavior

with low coercivity and remanence, similar to MBBS-35, and a magnetic saturation (M_s) value of 48.6 emu g^{-1} (Table S2, Supplementary Materials). It can be observed a reduction in M_s of MBBS@mSiO₂ compared to uncovered MBBS-35 ($M_s = 75.4 \text{ emu g}^{-1}$), which is often attributed to presence of the diamagnetic silica [44].

The preparation of MBBS@TiO₂ was carried out via the sol-gel method using titanium (IV) butoxide (TBOT) as precursor of TiO₂. Noteworthy, no additional stabilizers/templates were used in the synthesis processes. TEM images of MBBS@TiO₂ showed the successful formation of a homogeneous TiO₂ layer on the surface of the IONPs with a thickness ranging between 15 and 33 nm (Figure 6 and Figure S8, Supplementary Materials). In this case, the hydroxyl and carboxylic groups of MBBS can promote intermolecular interactions with TBOT, leading to a uniform deposition of the TiO₂ layer onto the BBS-coated IONPs. The XRD pattern of MBBS@TiO₂ (Figure S9, Supplementary Materials) evidenced the formation of anatase as the only TiO₂ crystalline phase in the nanoparticles. Additionally, hematite ($\alpha\text{-Fe}_2\text{O}_3$) and Fe₃O₄ were detected in the XRD diffraction pattern, which indicates that some oxidation degree of IONPs occurred in the calcination process at 500 °C. Magnetic curves obtained at 300 K clearly revealed a superparamagnetic behavior for MBBS@TiO₂ with a M_s value of 19.7 emu g^{-1} (Figure S7, Supplementary Materials). This lower M_s value compared to MBBS-35 can be explained by the presence of non-magnetic phases, such as the TiO₂ layer and hematite. Despite this, MBBS@TiO₂ nanoparticles possess a strong magnetic response and can be easily recovered by applying an external magnetic field.

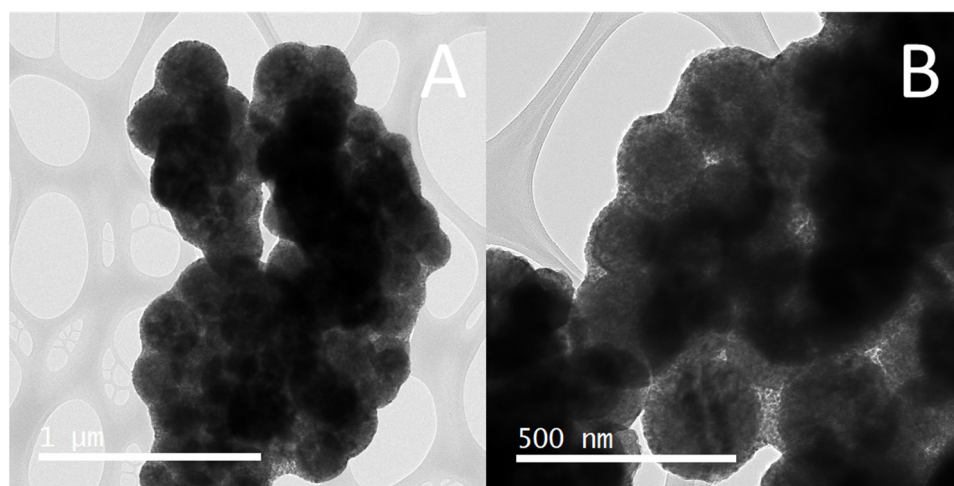


Figure 6. (A,B) TEM images of MBBS@TiO₂.

Magnetic core@shell nanoparticles have a wide range of applications in different research fields. In particular, due to its remarkable surface and magnetic features, MBBS@mSiO₂ raw or functionalized is a promising material for technological applications, such as adsorption [45,46], chromatography [47], and drug delivery [39], whereas MBBS@TiO₂ is a promising photocatalyst for environmental remediation [48]. In this study, we tested two potential applications of MBBS@mSiO₂, as a drug carrier and as adsorbent of pollutants from aqueous media.

The drug cargo capacity of MBBS@mSiO₂ by using ibuprofen (IBU), a well-known anti-inflammatory drug, was performed. The drug loading capacity, DLC (%) was defined as follows:

$$\text{DLC (\%)} = (\text{mass of IBU released} / \text{mass of nanoparticles}) \times 100 \quad (1)$$

Figure 7A shows the gradual release of IBU from MBBS@mSiO₂ at different times. The DLC of MBBS@mSiO₂ results to be around 13%, making them a good candidate as a drug delivery system. To better control the IBU release, the surface of MBBS@mSiO₂ should be modified with appropriate release triggers that specifically react with response

to stimuli [49]. Thus, MBBS@mSiO₂ could be a potential starting material for a subsequent modification that results in a controlled drug delivery system.

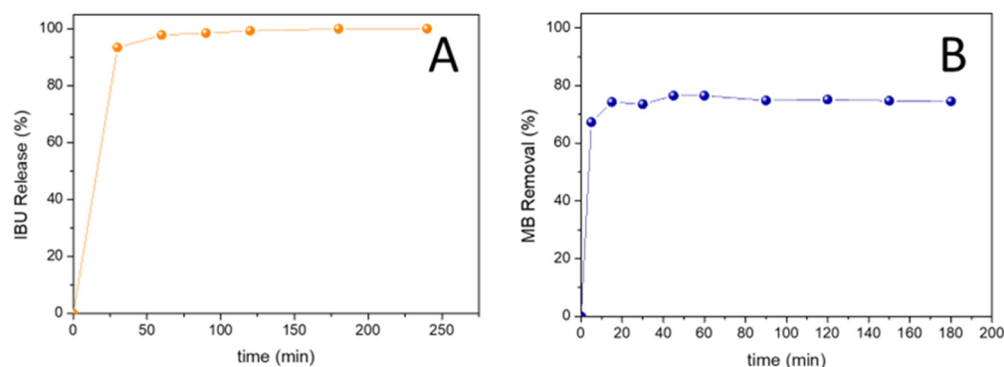


Figure 7. (A) Ibuprofen release from MBBS@mSiO₂ (T = 25 °C pH = 6.0) (B) MB removal from water using MBBS@mSiO₂ as adsorbent ([MB]₀ = 10 mg L⁻¹; MBBS@mSiO₂ dosage = 500 mg L⁻¹, T = 25 °C pH = 6.0).

On the other hand, MBBS@mSiO₂ was tested as adsorbent for the removal of methylene blue (MB), a toxic cationic dye that is used in textile industry. Figure 7B shows the % MB removal at different times. A very fast adsorption of MB can be observed, achieving a 76% dye removal in the first 15 min. Figure S10, Supplementary Materials, shows the evolution of UV-Vis spectra of MB at different times. The adsorption capacity of MB found for MBBS@mSiO₂ was similar to those of other magnetic mesoporous silicas reported in the literature [45].

MBBS@TiO₂ was studied as photocatalyst for the degradation of MB. Figure S11, Supplementary Materials, shows the evolution of the UV-Vis spectra of MB solution when irradiated in the presence of MBBS@TiO₂. The absorbance values at 664 nm were used to follow the MB photobleaching kinetics. For comparison purpose, MB photodegradation experiments were also carried out with TiO₂ synthesized in the absence of IONPs nanoparticles, but keeping the rest of the synthesis parameters unchanged. In these photocatalytic experiments, the same load of TiO₂ was used, so it was considered that MBBS@TiO₂ have an approximately composition of 33 wt.% of TiO₂. This composition was roughly estimated from the average size of cores and shells determined by TEM and the densities of pristine Fe₃O₄ and TiO₂. Figure 8 compares the evolution of the normalized absorbance at 664 nm with the reaction time obtained for MB degradation performed with MBBS@TiO₂ and TiO₂. It can be seen that MBBS@TiO₂ is capable of degrading MB with the same efficiency of pristine TiO₂. This is an excellent result, since a direct contact between Fe₃O₄ and TiO₂ typically brings about an unfavorable heterojunction, which accelerates the recombination of the electron-hole pairs and weakens the photocatalytic activity of titanium-based catalysts [50]. It was reported that the addition of a silica layer between an iron oxide core and a titania shell promotes the photocatalytic activity by decreasing the charge transfer between the IONPs and TiO₂, which could otherwise result in the recombination of photogenerated species on the IONPs surface [51]. Therefore, in our case, it is probable that BBS avoid the formation of a Fe₃O₄/TiO₂ heterojunction.

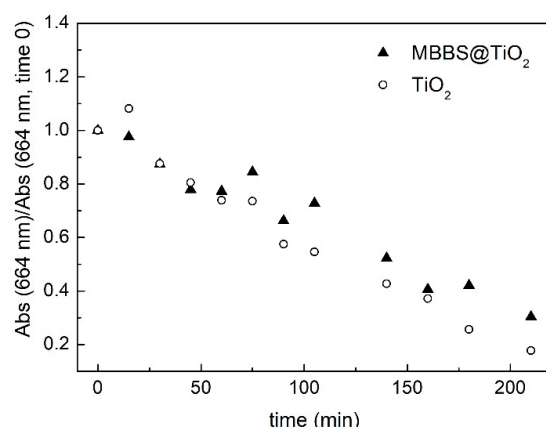


Figure 8. Photocatalytic activities of MBBS@TiO₂ and TiO₂. [MB]₀ = 5 mg L⁻¹; load MBBS@TiO₂ = 120 mg L⁻¹; load TiO₂ = 40 mg L⁻¹; pH = 6.

3. Materials and Methods

3.1. Reagents

FeCl₃·6H₂O (>99%) was purchased from Anedra (Buenos Aires, Argentina). Sodium acetate trihydrate (99%), ammonia solution (25–30%), and absolute ethanol were obtained from Cicarelli (Santa Fe, Argentina). Cetyltrimethylammonium bromide (CTAB, >97%) was purchased from Merck (Burlington, MA, USA). Ibuprofen, Tetraethoxysilane (TEOS, 98%) and titanium (IV) butoxide (TBOT, 97%) were from Sigma-Aldrich (Burlington, MA, USA). Acetonitrile (HPLC grade) was purchased from Biopack (Worcester, UK). All reactants were used without further purification. BBS were obtained following a previously reported protocol [22]; briefly, 50 g of green compost was treated with 1 L of 6 M NaOH aqueous solution under stirring at 60 °C for 4 h. The reaction mixture was then separated by centrifugation. The supernatant was concentrated, and different fractions were separated through a lab-scale ultrafiltration unit equipped with a membrane (molar mass cut-off 5 kDa). The retentate fraction was then dried at 60 °C for 24 h. The obtained BBS was about 20–30% in mass of the starting compost. Chemical composition of BBS is detailed in Table S4, in the Supplementary Material.

3.2. Synthesis of IONPs and Core-Shell Magnetic Nanoparticles

The synthesis of magnetite nanoparticles was performed by a modification of the polyol method [52]. Briefly, 1.35 g of FeCl₃·6H₂O, 6 g of sodium acetate trihydrate and a defined mass of BBS (35 mg, 70 mg, 200 mg, 500 mg and 1000 mg) were dissolved in a Teflon vessel containing 50 mL of ethylene glycol. Thereafter, the Teflon vessel was placed into a stainless-steel autoclave reactor and heated at 200 °C for 8 h. Once cooled, the obtained black material was washed with ethanol and water. The solid was separated from the supernatant with the assistance of a Neodymium magnet in all washing steps. The obtained materials were named as MBBS-35, MBBS-70, MBBS-200, MBBS-500, and MBBS-1000 depending on the amount of BBS used in the synthesis process. Additionally, Fe₃O₄ without BBS was prepared with the same method as a reference material.

The covering of MBBS-35 with a mesoporous silica shell (MBBS@mSiO₂) was performed following our previous report [53]. In brief, 400 mg of MBBS-35, 500 mg of CTAB and 1.75 mL of ammonia solution were mixed in 250 mL of water. The suspension was kept under vigorous stirring and heating for 30 min. When the temperature reached 80 °C, 2.5 mL of TEOS was added drop by drop and the reaction was kept at 80 °C for 2 h. After cooling, the obtained material was magnetically separated, washed with distilled water and dried in an oven at 70 °C overnight. Finally, CTAB and BBS were removed by calcination in a furnace (500 °C for 1 h in air) and the final product was named as MBBS@mSiO₂.

MBBS-35 coating with titanium dioxide shell (MBBS@TiO₂) was performed via a sol-gel method [54]. For this, 50 mg of MBBS-35 were dispersed by sonication in a mixture

of 90 mL absolute ethanol/30 mL acetonitrile. Then, 0.5 mL of ammonia solution and 1.0 mL of TBOT was added and the dispersion was kept under stirring at 25 °C for 1.5 h. Later, the sample was washed with ethanol, magnetically separated and dried at 70 °C. Then, the obtained material was calcined in argon atmosphere at 500 °C for 9 h. Pure TiO₂ nanoparticles were also prepared for comparison.

3.3. Application of Core-Shell Magnetic Nanoparticles

MBBS@mSiO₂ was evaluated as potential drug carrier. For this end, the drug loading capacity (DLC) using ibuprofen as model drug was measured according to our previous report [53]. First, MBBS@SiO₂ were loaded with IBU. For this, 20 mg of nanoparticles were dispersed in a hexane solution of IBU (0.16 M) and the system was kept under magnetic stirring in a closed flask for 24 h. Afterwards, the nanoparticles were magnetically separated from the supernatant and washed once with hexane. Later, a release of ibuprofen assay was conducted. For this purpose, fresh 0.9% NaCl was added to the flask containing the loaded nanoparticles. The system was stirred and at defined times an aliquot was magnetically separated and measured in a UV spectrophotometer (UV-T60, PG Instruments, Leicestershire, UK) to quantify the released amount of IBU ($\lambda = 264$ nm).

The photocatalytic activity of MBBS@TiO₂ was tested via the degradation of aqueous solutions of methylene blue (MB). The photochemical experiments were performed in a 200 mL cylindrical Pyrex vessel at room temperature and under continuous stirring. A solar simulator (SunLite™, ABET Technologies, Milford, CT, USA) equipped with a 100 W Xenon Short Arc Lamp was used as irradiation source. In all the experiments, the initial concentration of MB was 5 mg L⁻¹, and the load of the photocatalyst were 120 mg L⁻¹ and 40 mg L⁻¹ for MBBS@TiO₂ and TiO₂, respectively. The aqueous suspensions were irradiated for 4 h, and 3 mL aliquots were taken at different times. The separation of the supernatant was achieved by magnetic separation. Finally, the residual MB concentration was determined by UV-Vis Spectrophotometry.

3.4. Characterization Techniques

Transmission electron microscopy (TEM) images were obtained using a Tecnai F20 (G2) UT microscope (ThermoFisher, Waltham, MA, USA), operated at 200 kV. X-ray diffraction (XRD) patterns were obtained on a SmartLab SE 3 KW (Rigaku, Tokyo, Japan) equipped with Cu anode (45 kV, 40 mA) and a graphite monochromator. Fourier transform infrared (FTIR) spectra were recorded by using an FT-08 spectrophotometer (Lumex, Wakendorf II, Germany) on KBr pellets (1/300 wt.) in transmission mode with 128 scans at 4 cm⁻¹ resolution. Thermogravimetric analysis (TGA) was performed with a TGA-DSC Q600 Thermogravimetric Analyzer (TA Instruments, New Castle, DE, USA). The samples were pre-dried for 30 min at 100 °C before the analysis (heating rate of 10 °C min⁻¹ from room temperature to 1000 °C in air). The analysis of textural properties was conducted with N₂ adsorption/desorption isotherms on previously degassed samples (105 °C for 12 h) at 77 K using an ASAP 2000 sorptometer (Micromeritics, Norcross, GA, USA). The specific surface area was calculated via the Brunauer-Emmett-Teller (BET) method, the pore volume was calculated using Gurvich's rule at relative pressure $p/p_0 = 0.98$ and the pore size distribution was calculated according to the Barrett-Joyner-Halenda (BJH) method. Magnetization curves were registered at 300 K by using 7300 vibrating sample magnetometer (LakeShore, Westerville, OH, USA). The zeta potential measurements were carried out by using a zetasizer nano (Malvern Instruments, Malvern, UK).

4. Conclusions

A novel procedure based on the polyol method was applied for the synthesis of IONPs stabilized with BBS. TEM images show that both the size of the nanocrystals and their aggregation strongly depend on the BBS concentration used in the synthesis. In particular, under the conditions employed for the preparation of MBBS-35 particles, well-defined roughly spherical clusters with diameters of about 70–200 nm are observed.

BBS were also employed as nucleation directing agents in the synthesis of nanostructured core-shell MBBS@SiO₂ and MBBS@TiO₂ nanoparticles. Our results indicate that the obtained nanostructured magnetic core-shell nanomaterials using BBS can successfully be applied with good performance in different systems. In particular, MBBS@SiO₂ showed to be an excellent nanocarrier of ibuprofen. The material achieves a 13% of drug loading capacity and around 90% of the cargo was released within 90 min. MBBS@SiO₂ also were successfully employed as adsorbents for the quantitative removal of methylene blue from aqueous solution. On the other hand, MBBS@TiO₂ was capable of degrading MB with the same efficiency of pristine TiO₂. This excellent result shows that the BBS layer that covers the IONPs avoids formation of the unfavorable heterojunction between Fe₃O₄ and TiO₂.

Supplementary Materials: The following supporting information can be downloaded at: <https://www.mdpi.com/article/10.3390/inorganics11010046/s1>, Figure S1. Particle size distribution obtained from TEM images; Figure S2: High resolution TEM image of MBBS-35; Figure S3: High resolution TEM image of MBBS-1000; Figure S4: Magnetization curves (300 K) of Fe₃O₄ and covered magnetite with different amount of BBS; Figure S5: FTIR spectra of MBBS@mSiO₂ material; Figure S6: (A) N₂ adsorption/desorption isotherms of MBBS-35 and of MBBS@SiO₂ (B) pore-size distribution of MBBS@SiO₂; Figure S7: Magnetization curves at 300 K of MBBS@mSiO₂ and MBBS@TiO₂; Figure S8. High resolution TEM image of MBBS@TiO₂. Red lines indicate the thickness of TiO₂ layer; Figure S9: XRD diffraction pattern of MBBS@TiO₂. M (Magnetite), A (Anatase), and H (Hematite).; Figure S10. UV-Vis absorption spectra of aqueous solutions of MB at different contact times using MBBS@mSiO₂ as adsorbent. ([MB]₀ = 10 mg L⁻¹; MBBS@mSiO₂ dosage = 500 mg L⁻¹, T = 25 °C pH = 6.0); Figure S11. UV-Vis absorption spectra of aqueous solutions of MB at different irradiation times using MBBS@TiO₂ as photocatalyst. ([MB]₀ = 5 mg L⁻¹; load MBBS@TiO₂ = 120 mg L⁻¹; load TiO₂ = 40 mg L⁻¹; pH = 6; Table S1: Total mass loss calculated by TGA for MBBS-X samples; Table S2: Magnetic properties of nanostructured core-shell prepared materials; Table S3: Zeta potential measurements of BBS coated magnetic iron oxide nanoparticles. Table S4: Chemical composition of BBS.

Author Contributions: Conceptualization, M.E.P. and L.C.; methodology, M.E.P. and A.K.-F.; investigation, M.E.P., A.K.-F. and M.S.M.; writing—original draft preparation, M.E.P., D.O.M. and L.C.; writing—review and editing, M.E.P., D.O.M. and L.C.; project administration, D.O.M., M.S.M. and L.C.; funding acquisition, D.O.M., M.S.M. and L.C. All authors have read and agreed to the published version of the manuscript.

Funding: This research was funded by ANPCyT (PICT-1847-2017), UNCo (PIP 04/L009), and CONICET (PIP 11220200100768CO).

Data Availability Statement: Not applicable.

Acknowledgments: Authors would like to thank Giuliana Magnacca (UNITO, Italy) for providing BBS samples. M.E. Peralta thank CONICET for his postdoc grant. L. Carlos and M.S. Moreno are research members of CONICET (Argentina). D. Mártire is a research member of CIC (Buenos Aires, Argentina).

Conflicts of Interest: The authors declare no conflict of interest. The funders had no role in the design of the study; in the collection, analyses, or interpretation of data; in the writing of the manuscript; or in the decision to publish the results.

References

1. Nisticò, R.; Cesano, F.; Garello, F. Magnetic Materials and Systems: Domain Structure Visualization and Other Characterization Techniques for the Application in the Materials Science and Biomedicine. *Inorganics* **2020**, *8*, 6. [[CrossRef](#)]
2. Pathak, S.; Jain, K.; Kumar, P.; Wang, X.; Pant, R.P. Improved Thermal Performance of Annular Fin-Shell Tube Storage System Using Magnetic Fluid. *Appl. Energy* **2019**, *239*, 1524–1535. [[CrossRef](#)]
3. Pathak, S.; Jain, K.; Kumar, V.; Pant, R.P. Magnetic Fluid Based High Precision Temperature Sensor. *IEEE Sens. J.* **2017**, *17*, 2670–2675. [[CrossRef](#)]
4. Noh, B.-I.; Yang, S.C. Ferromagnetic, Ferroelectric, and Magnetoelectric Properties in Individual Nanotube-Based Magnetoelectric Films of CoFe₂O₄/BaTiO₃ Using Electrically Resistive Core-Shell Magnetostrictive Nanoparticles. *J. Alloys Compd.* **2022**, *891*, 161861. [[CrossRef](#)]

5. Peralta, M.E.; Ocampo, S.; Funes, I.G.; Medina, F.O.; Parolo, M.E.; Carlos, L. Nanomaterials with Tailored Magnetic Properties as Adsorbents of Organic Pollutants from Wastewaters. *Inorganics* **2020**, *8*, 24. [[CrossRef](#)]
6. Nisticò, R. Magnetic Materials and Water Treatments for a Sustainable Future. *Res. Chem. Intermed.* **2017**, *43*, 6911–6949. [[CrossRef](#)]
7. Carlos, L.; Garcia Einschlag, F.S.; González, M.C.; Mártire, D.O. Applications of Magnetite Nanoparticles for Heavy Metal Removal from Wastewater. In *Waste Water—Treatment Technologies and Recent Analytical Developments*; IntechOpen: London, UK, 2013; pp. 1–16. [[CrossRef](#)]
8. Fotukian, S.M.; Barati, A.; Soleymani, M.; Alizadeh, A.M. Solvothermal Synthesis of CuFe_2O_4 and Fe_3O_4 Nanoparticles with High Heating Efficiency for Magnetic Hyperthermia Application. *J. Alloys Compd.* **2020**, *816*, 152548. [[CrossRef](#)]
9. Liu, H.; Ji, S.; Zheng, Y.; Li, M.; Yang, H. Modified Solvothermal Synthesis of Magnetic Microspheres with Multifunctional Surfactant Cetyltrimethyl Ammonium Bromide and Directly Coated Mesoporous Shell. *Powder Technol.* **2013**, *246*, 520–529. [[CrossRef](#)]
10. Cheng, C.; Wen, Y.; Xu, X.; Gu, H. Tunable Synthesis of Carboxyl-Functionalized Magnetite Nanocrystal Clusters with Uniform Size. *J. Mater. Chem.* **2009**, *19*, 8782. [[CrossRef](#)]
11. Liu, J.; Sun, Z.; Deng, Y.; Zou, Y.; Li, C.; Guo, X.; Xiong, L.; Gao, Y.; Li, F.; Zhao, D. Highly Water-Dispersible Biocompatible Magnetite Particles with Low Cytotoxicity Stabilized by Citrate Groups. *Angew. Chemie Int. Ed.* **2009**, *48*, 5875–5879. [[CrossRef](#)]
12. Wang, W.; Tang, B.; Ju, B.; Zhang, S. Size-Controlled Synthesis of Water-Dispersible Superparamagnetic Fe_3O_4 Nanoclusters and Their Magnetic Responsiveness. *RSC Adv.* **2015**, *5*, 75292–75299. [[CrossRef](#)]
13. Deng, H.; Li, X.; Peng, Q.; Wang, X.; Chen, J.; Li, Y. Monodisperse Magnetic Single-Crystal Ferrite Microspheres. *Angew. Chem.* **2005**, *117*, 2842–2845. [[CrossRef](#)]
14. Ge, J.; Hu, Y.; Biasini, M.; Beyermann, W.P.; Yin, Y. Superparamagnetic Magnetite Colloidal Nanocrystal Clusters. *Angew. Chemie Int. Ed.* **2007**, *46*, 4342–4345. [[CrossRef](#)]
15. Liang, J.; Ma, H.; Luo, W.; Wang, S. Synthesis of Magnetite Submicrospheres with Tunable Size and Superparamagnetism by a Facile Polyol Process. *Mater. Chem. Phys.* **2013**, *139*, 383–388. [[CrossRef](#)]
16. Liu, Y.; Cui, T.; Li, Y.; Zhao, Y.; Ye, Y.; Wu, W.; Tong, G. Effects of Crystal Size and Sphere Diameter on Static Magnetic and Electromagnetic Properties of Monodisperse Fe_3O_4 Microspheres. *Mater. Chem. Phys.* **2016**, *173*, 152–160. [[CrossRef](#)]
17. Li, S.; Zhang, T.; Tang, R.; Qiu, H.; Wang, C.; Zhou, Z. Solvothermal Synthesis and Characterization of Monodisperse Superparamagnetic Iron Oxide Nanoparticles. *J. Magn. Magn. Mater.* **2015**, *379*, 226–231. [[CrossRef](#)]
18. Montoneri, E.; Prevot, A.B.; Avetta, P.; Arques, A.; Carlos, L.; Magnacca, G.; Laurenti, E.; Tabasso, S. CHAPTER 4: Food Wastes Conversion to Products for Use in Chemical and Environmental Technology, Material Science and Agriculture. In *RSC Green Chemistry*; Royal Society of Chemistry: London, UK, 2013; pp. 64–109. ISBN 9781849736152.
19. Quagliotto, P.; Montoneri, E.; Tambone, F.; Adani, F.; Gobetto, R.; Viscardi, G. Chemicals from Wastes: Compost-Derived Humic Acid-like Matter as Surfactant. *Environ. Sci. Technol.* **2006**, *40*, 1686–1692. [[CrossRef](#)]
20. Boffa, V.; Perrone, D.G.; Montoneri, E.; Magnacca, G.; Bertinetti, L.; Garlasco, L.; Mendichi, R. A Waste-Derived Biosurfactant for the Preparation of Templated Silica Powders. *ChemSusChem* **2010**, *3*, 445–452. [[CrossRef](#)]
21. Nisticò, R.; Carlos, L. High Yield of Nano Zero-Valent Iron (NZVI) from Carbothermal Synthesis Using Lignin-Derived Substances from Municipal Biowaste. *J. Anal. Appl. Pyrolysis* **2019**, *140*, 239–244. [[CrossRef](#)]
22. Nisticò, R.; Barrasso, M.; Carrillo Le Roux, G.A.; Seckler, M.M.; Sousa, W.; Malandrino, M.; Magnacca, G. Biopolymers from Composted Biowaste as Stabilizers for the Synthesis of Spherical and Homogeneously Sized Silver Nanoparticles for Textile Applications on Natural Fibers. *ChemPhysChem* **2015**, *16*, 3902–3909. [[CrossRef](#)] [[PubMed](#)]
23. Magnacca, G.; Allera, A.; Montoneri, E.; Celi, L.; Benito, D.E.; Gagliardi, L.G.; Gonzalez, M.C.; Mártire, D.O.; Carlos, L. Novel Magnetite Nanoparticles Coated with Waste-Sourced Biobased Substances as Sustainable and Renewable Adsorbing Materials. *ACS Sustain. Chem. Eng.* **2014**, *2*, 1518–1524. [[CrossRef](#)]
24. Nisticò, R.; Cesano, F.; Franzoso, F.; Magnacca, G.; Scarano, D.; Funes, I.G.; Carlos, L.; Parolo, M.E. From Biowaste to Magnet-Responsive Materials for Water Remediation from Polycyclic Aromatic Hydrocarbons. *Chemosphere* **2018**, *202*, 686–693. [[CrossRef](#)]
25. Nisticò, R.; Celi, L.R.; Bianco Prevot, A.; Carlos, L.; Magnacca, G.; Zanzo, E.; Martin, M. Sustainable Magnet-Responsive Nanomaterials for the Removal of Arsenic from Contaminated Water. *J. Hazard. Mater.* **2018**, *342*, 260–269. [[CrossRef](#)]
26. Franzoso, F.; Nisticò, R.; Cesano, F.; Corazzari, I.; Turci, F.; Scarano, D.; Bianco Prevot, A.; Magnacca, G.; Carlos, L.; Mártire, D.O. Biowaste-Derived Substances as a Tool for Obtaining Magnet-Sensitive Materials for Environmental Applications in Wastewater Treatments. *Chem. Eng. J.* **2017**, *310*, 307–316. [[CrossRef](#)]
27. Aparicio, F.; Mizrahi, M.; Ramallo-López, J.M.; Laurenti, E.; Magnacca, G.; Carlos, L.; Mártire, D.O. Novel Bimetallic Magnetic Nanocomposites Obtained from Waste-Sourced Bio-Based Substances as Sustainable Photocatalysts. *Mater. Res. Bull.* **2022**, *152*, 111846. [[CrossRef](#)]
28. Ayala, L.I.M.; Aparicio, F.; Boffa, V.; Magnacca, G.; Carlos, L.; Bosio, G.N.; Mártire, D.O. Removal of As(III) via Adsorption and Photocatalytic Oxidation with Magnetic Fe–Cu Nanocomposites. *Photochem. Photobiol. Sci.* **2022**, *1*, 1–10. [[CrossRef](#)] [[PubMed](#)]
29. Ou, X.; Chen, S.; Quan, X.; Zhao, H. Photochemical Activity and Characterization of the Complex of Humic Acids with Iron(III). *J. Geochem. Explor.* **2009**, *102*, 49–55. [[CrossRef](#)]
30. Yadav, R.S.; Havlica, J.; Kuřitka, I.; Kozakova, Z.; Masilko, J.; Hajdúchová, M.; Enev, V.; Wasserbauer, J. Effect of Pr^{3+} Substitution on Structural and Magnetic Properties of CoFe_2O_4 Spinel Ferrite Nanoparticles. *J. Supercond. Nov. Magn.* **2015**, *28*, 241–248. [[CrossRef](#)]

31. Arun, T.; Prabakaran, K.; Udayabhaskar, R.; Mangalaraja, R.V.; Akbari-Fakhrabadi, A. Carbon Decorated Octahedral Shaped Fe_3O_4 and $\alpha\text{-Fe}_2\text{O}_3$ Magnetic Hybrid Nanomaterials for next Generation Supercapacitor Applications. *Appl. Surf. Sci.* **2019**, *485*, 147–157. [[CrossRef](#)]
32. Shirsath, S.E.; Kadam, R.H.; Mane, M.L.; Ghasemi, A.; Yasukawa, Y.; Liu, X.; Morisako, A. Permeability and Magnetic Interactions in Co^{2+} Substituted $\text{Li}_{0.5}\text{Fe}_{2.5}\text{O}_4$ Alloys. *J. Alloys Compd.* **2013**, *575*, 145–151. [[CrossRef](#)]
33. Vargas, J.M.; Shukla, D.K.; Meneses, C.T.; Mendoza Zélis, P.; Singh, M.; Sharma, S.K. Synthesis, Phase Composition, Mössbauer and Magnetic Characterization of Iron Oxide Nanoparticles. *Phys. Chem. Chem. Phys.* **2016**, *18*, 9561–9568. [[CrossRef](#)]
34. Kim, W.; Suh, C.Y.; Cho, S.W.; Roh, K.M.; Kwon, H.; Song, K.; Shon, I.J. A New Method for the Identification and Quantification of Magnetite-Maghemite Mixture Using Conventional X-Ray Diffraction Technique. *Talanta* **2012**, *94*, 348–352. [[CrossRef](#)] [[PubMed](#)]
35. Cuenca, J.A.; Bugler, K.; Taylor, S.; Morgan, D.; Williams, P.; Bauer, J.; Porch, A. Study of the Magnetite to Maghemite Transition Using Microwave Permittivity and Permeability Measurements. *J. Phys. Condens. Matter* **2016**, *28*, 106002. [[CrossRef](#)]
36. Arun, T.; Prakash, K.; Kuppasamy, R.; Joseyphus, R.J. Magnetic Properties of Prussian Blue Modified Fe_3O_4 Nanocubes. *J. Phys. Chem. Solids* **2013**, *74*, 1761–1768. [[CrossRef](#)]
37. Dutta, P.; Pal, S.; Seehra, M.S.; Shah, N.; Huffman, G.P. Size Dependence of Magnetic Parameters and Surface Disorder in Magnetite Nanoparticles. *J. Appl. Phys.* **2009**, *105*, 10–13. [[CrossRef](#)]
38. Peralta, M.E.; Nisticò, R.; Franzoso, F.; Magnacca, G.; Fernandez, L.; Parolo, M.E.; León, E.G.; Carlos, L. Highly Efficient Removal of Heavy Metals from Waters by Magnetic Chitosan-Based Composite. *Adsorption* **2019**, *25*, 1337–1347. [[CrossRef](#)]
39. Zhao, Q.; Xie, P.; Li, X.; Wang, Y.; Zhang, Y.; Wang, S. Magnetic Mesoporous Silica Nanoparticles Mediated Redox and PH Dual-Responsive Target Drug Delivery for Combined Magnetothermal Therapy and Chemotherapy. *Colloids Surf. A Physicochem. Eng. Asp.* **2022**, *648*, 129359. [[CrossRef](#)]
40. Kamarudin, N.H.N.; Jalil, A.A.; Triwahyono, S.; Sazegar, M.R.; Hamdan, S.; Baba, S.; Ahmad, A. Elucidation of Acid Strength Effect on Ibuprofen Adsorption and Release by Aluminated Mesoporous Silica Nanoparticles. *RSC Adv.* **2015**, *5*, 30023–30031. [[CrossRef](#)]
41. Bian, Q.; Xue, Z.; Sun, P.; Shen, K.; Wang, S.; Jia, J. Visible-Light-Triggered Supramolecular Valves Based on β -Cyclodextrin-Modified Mesoporous Silica Nanoparticles for Controlled Drug Release. *RSC Adv.* **2019**, *9*, 17179–17182. [[CrossRef](#)]
42. Thommes, M.; Kaneko, K.; Neimark, A.V.; Olivier, J.P.; Rodriguez-Reinoso, F.; Rouquerol, J.; Sing, K.S.W. Physisorption of Gases, with Special Reference to the Evaluation of Surface Area and Pore Size Distribution (IUPAC Technical Report). *Pure Appl. Chem.* **2015**, *87*, 1051–1069. [[CrossRef](#)]
43. Jin, C.; Wang, Y.; Wei, H.; Tang, H.; Liu, X.; Lu, T.; Wang, J. Magnetic Iron Oxide Nanoparticles Coated by Hierarchically Structured Silica: A Highly Stable Nanocomposite System and Ideal Catalyst Support. *J. Mater. Chem. A* **2014**, *2*, 11202–11208. [[CrossRef](#)]
44. Hou, X.; Xu, H.; Pan, L.; Tian, Y.; Zhang, X.; Ma, L.; Li, Y.; Zhao, J. Adsorption of Bovine Serum Albumin on Superparamagnetic Composite Microspheres with a $\text{Fe}_3\text{O}_4/\text{SiO}_2$ Core and Mesoporous SiO_2 Shell. *RSC Adv.* **2015**, *5*, 103760–103766. [[CrossRef](#)]
45. Nicola, R.; Muntean, S.G.; Nistor, M.A.; Putz, A.M.; Almásy, L.; Săcărescu, L. Highly Efficient and Fast Removal of Colored Pollutants from Single and Binary Systems, Using Magnetic Mesoporous Silica. *Chemosphere* **2020**, *261*, 127737. [[CrossRef](#)]
46. Nicola, R.; Costişor, O.; Muntean, S.G.; Nistor, M.A.; Putz, A.M.; Ianăşi, C.; Lazău, R.; Almásy, L.; Săcărescu, L. Mesoporous Magnetic Nanocomposites: A Promising Adsorbent for the Removal of Dyes from Aqueous Solutions. *J. Porous Mater.* **2020**, *27*, 413–428. [[CrossRef](#)]
47. Jiang, Y.; Liang, W.; Wang, B.; Feng, Q.; Xia, C.; Wang, Q.; Yan, Y.; Zhao, L.; Cui, W.; Liang, H. Magnetic Mesoporous Silica Nanoparticles Modified by Phosphate Functionalized Ionic Liquid for Selective Enrichment of Phosphopeptides. *RSC Adv.* **2022**, *12*, 26859–26865. [[CrossRef](#)]
48. Gómez-Pastora, J.; Dominguez, S.; Bringas, E.; Rivero, M.J.; Ortiz, I.; Dionysiou, D.D. Review and Perspectives on the Use of Magnetic Nanophotocatalysts (MNPCs) in Water Treatment. *Chem. Eng. J.* **2017**, *310*, 407–427. [[CrossRef](#)]
49. Salve, R.; Kumar, P.; Ngamcherdtrakul, W.; Gajbhiye, V.; Yantasee, W. Stimuli-Responsive Mesoporous Silica Nanoparticles: A Custom-Tailored next Generation Approach in Cargo Delivery. *Mater. Sci. Eng. C* **2021**, *124*, 112084. [[CrossRef](#)]
50. Wang, D.; Yang, J.; Li, X.; Wang, J.; Zhai, H.; Lang, J.; Song, H. Effect of Thickness and Microstructure of TiO_2 Shell on Photocatalytic Performance of Magnetic Separable $\text{Fe}_3\text{O}_4/\text{SiO}_2/\text{MTiO}_2$ Core-Shell Composites. *Phys. Status Solidi Appl. Mater. Sci.* **2017**, *214*, 1600665. [[CrossRef](#)]
51. Mamba, G.; Mishra, A. Advances in Magnetically Separable Photocatalysts: Smart, Recyclable Materials for Water Pollution Mitigation. *Catalysts* **2016**, *6*, 79. [[CrossRef](#)]
52. Deng, Y.; Qi, D.; Deng, C.; Zhang, X.; Zhao, D. Superparamagnetic High-Magnetization Microspheres with an $\text{Fe}_3\text{O}_4@\text{SiO}_2$ Core and Perpendicularly Aligned Mesoporous SiO_2 Shell for Removal of Microcystins. *J. Am. Chem. Soc.* **2008**, *130*, 28–29. [[CrossRef](#)]
53. Peralta, M.E.; Jadhav, S.A.; Magnacca, G.; Scalarone, D.; Mártire, D.O.; Parolo, M.E.; Carlos, L. Synthesis and in Vitro Testing of Thermoresponsive Polymer-Grafted Core-Shell Magnetic Mesoporous Silica Nanoparticles for Efficient Controlled and Targeted Drug Delivery. *J. Colloid Interface Sci.* **2019**, *544*, 198–205. [[CrossRef](#)] [[PubMed](#)]
54. Zhang, Q.; Meng, G.; Wu, J.; Li, D.; Liu, Z. Study on Enhanced Photocatalytic Activity of Magnetically Recoverable $\text{Fe}_3\text{O}_4@\text{C}@\text{TiO}_2$ Nanocomposites with Core-Shell Nanostructure. *Opt. Mater.* **2015**, *46*, 52–58. [[CrossRef](#)]

Disclaimer/Publisher’s Note: The statements, opinions and data contained in all publications are solely those of the individual author(s) and contributor(s) and not of MDPI and/or the editor(s). MDPI and/or the editor(s) disclaim responsibility for any injury to people or property resulting from any ideas, methods, instructions or products referred to in the content.